Nonlinear Decoupling Study of Piezoelectric 6-Degree-of-Freedom Accelerometer

Min Li, Jianhang Yang, Ke Jian, Lan Qin, Jingcheng Liu, Jun Liu

***Abstract*—Theoretically, a piezoelectric 6-degree-of-freedom accelerometer can measure six-dimensional acceleration values through linear operations. However, due to the influence of calibration equipment, signal conditioning devices, and materials, the output often exhibits nonlinear characteristics. In addition, the current fixed, non-feedback solution method cannot meet the sensor's measurement requirements, necessitating research into high-precision and efficient decoupling methods. First, the measurement principles of the piezoelectric 6-degree-of-freedom accelerometer are analyzed. Then, to enable adaptive decoupling based on nonlinear compensation, the linear decoupling model is adjusted using the sensitivity curve obtained from nonlinear fitting, with iterative updates to the solution matrix. Finally, to achieve high accuracy and efficiency, the number of iterations in the nonlinear compensation adaptive decoupling model is analyzed and optimized. The linear decoupling model is compared and evaluated against the existing nonlinear decoupling method. The errors from linear decoupling, neural network decoupling, and nonlinear compensation decoupling are analyzed. Experimental results show that, compared with linear decoupling and neural network decoupling, the nonlinear compensation decoupling model reduces the average solution error of linear acceleration from 0.1170% and 0.0690% to 0.0067%, and the average solution error of angular acceleration from 6.0185% and 2.2899% to 0.8989%. The time for linear decoupling is 0.000004 seconds, for neural network decoupling 0.02458 seconds, and for nonlinear compensation decoupling 0.00047 seconds, demonstrating the effectiveness and practicality of the adaptive decoupling algorithm with nonlinear compensation.**

***Index Terms*—6-degree-of-freedom accelerometer, decoupled, Nonlinear, Reparation**

Manuscript received May 20, 2024; revised February 12, 2025. This work is supported by two projects, the first is National Key Research and Development Program of China (Grant No.2022YFB3206700) and the second is Natural Science Foundation Project of China (Grant No. 52175494). At the same time, the work is completed by the Key Laboratory of Optoelectronic Technology and Systems of Ministry of Education, College of Optoelectronic Engineering, Chongqing University.

Min Li is a professor level senior engineer at the School of Optoelectronic Engineering, Chongqing University, Chongqing, 400044, P. R. China. (corresponding author to provide e-mail: limin780815@cqu.edu.cn).

Jianhang Yang is a postgraduate student at the School of Optoelectronic Engineering, Chongqing University, Chongqing, 400044, P. R. China. (e-mail:1447993258@qq.com).

Ke Jian is a postgraduate student at the School of Optoelectronic Engineering, Chongqing University, Chongqing, 400044, P. R. China. (e-mail: 20160813078@cqu.edu.cn).

Lan Qin is a professor at the School of Optoelectronic Engineering, Chongqing University, Chongqing, 400044, P. R. China. (e-mail: qinlan@cqu.edu.cn).

Jingcheng Liu is a professor at the School of Optoelectronic Engineering, Chongqing University, Chongqing, 400044, P. R. China. (e-mail: jingchengliu@cqu.edu.cn).

Jun Liu is a professor at the School of Optoelectronic Engineering, Chongqing University, Chongqing, 400044, P. R. China. (e-mail: junliu@cqu.edu.cn).

I. Introduction

FULL information dynamic parameter testing of six degrees of freedom (6-DOF) is critically important for the monitoring, prediction, control, and risk management of equipment and products operating in 6-DOF vibration environments, especially within aerospace and robotics. For instance, such testing is essential for satellite high-attitude jitter control, in-orbit engine vibration testing, and prediction of vibration faults in aircraft [1]. It is also relevant for the development of gyro-free strapdown inertial navigation systems capable of handling large attitude angles and high maneuver states [2][3][4]. Further applications include the complete decoupling of six-dimensional forces in robots, collaborative robot manpower control systems, and other scenarios requiring both linear and angular acceleration measurements [5]. The 6-DOF accelerometer is a novel sensor capable of simultaneously measuring linear acceleration along the X, Y, and Z axes, as well as angular acceleration across three axes.

As a multi-input and multi-output system, the 6-DOF accelerometer exhibits both linear and nonlinear coupling relationships between its inputs and outputs due to measurement principles, calibration equipment, and material influences. The coupling relationships involve more than 36 parameters, making decoupling a central research focus for 6-DOF accelerometers. Decoupling algorithms must ensure both high decoupling accuracy and efficiency to make these sensors viable for practical applications. Given the complexity of designing 6-DOF accelerometers and achieving effective decoupling, current research primarily focuses on static decoupling. For example, Yu et al. developed a linear decoupling method [6][7][8] for strain-based 6-DOF accelerometers using a Stewart platform structure, achieving a linear acceleration decoupling error of 2.6%. However, limitations in experimental equipment precluded testing of angular acceleration, and decoupling time was not reported. Subsequently, the team proposed a gray-box extreme learning machine decoupling algorithm [9] employing sparrow search for nonlinear decoupling of parallel six-dimensional accelerometers, achieving a maximum class I error of 0.023%, a class II error of 0.046%, and a decoupling time of 1.095 seconds. You et al. developed a decoupling algorithm for a six-degree-of-freedom accelerometer based on a 12-link preloaded parallel mechanism. By integrating the dynamic equations with the decoupling algorithm in a four-dimensional configuration space, a relative error of 0.62% was achieved, confirming the feasibility of the design [10]. Later, the same group of people constructed decoupling algorithms across bitmap, phase, and hybrid spaces to assess the impact of output errors, initial moment alignment errors, and decoupling parameter identification errors on the accuracy of sensitive elements in a

6-DOF accelerometer based on a 12-6-body Stewart platform, achieving a maximum laboratory static decoupling relative error of 8.87% and a decoupling time of 4.6 seconds [11][12]. Later, this team introduced a synthesis method [13] for configuring the Stewart-type six-dimensional acceleration sensing mechanism. This method applies the Newton-Euler approach to establish forward decoupling equations, analyzes the isotropy, and formulates a configuration synthesis procedure. The resulting 12-6 Stewart mechanism achieved a maximum citation error of 0.169% in virtual experiments, confirming its excellent isotropic performance. Zhang et al. developed a dynamic decoupling method [14] for parallel six-dimensional acceleration-sensing mechanisms. By analyzing the scale constraints of hinge points, they constructed an output coordination equation for the 12-6 mechanism and solved the forward decoupling equation for two configurations. Experimental results showed the method's effectiveness, achieving real-time decoupling with maximum citation errors of 4.23% and 6.53%, respectively. In summary, existing decoupling methods fall short in meeting the accuracy and efficiency requirements necessary for practical measurement applications with 6-DOF accelerometers. Therefore, there is an urgent need to develop high-accuracy, high-speed decoupling algorithms for 6-DOF accelerometers.

In this paper, we address the static decoupling challenges of a piezoelectric 6-DOF accelerometer by proposing both a linear decoupling model and a nonlinear adaptive decoupling model, building on the analysis of the measurement principles of the six-output piezoelectric 6-DOF accelerometer developed by our team [15][16][17]. Experimental results verify the effectiveness of both models. We compare and analyze the decoupling accuracy and speed of the linear decoupling model, the nonlinear adaptive decoupling model, and a neural network model, demonstrating that the nonlinear adaptive decoupling model enhances decoupling accuracy while achieving real-time measurement speeds. These findings offer new insights into adaptive decoupling for six-output piezoelectric 6-DOF accelerometers.

II. PIEZOELECTRIC 6-DOF ACCELEROMETER'S MEASUREMENT PRINCIPLE

Figure 1 illustrates the structure of the six-output piezoelectric 6-DOF accelerometer. This accelerometer uses piezoelectric quartz as the sensing element and comprises a cover (1), a pre-tensioning bolt (2), an inertial mass block (3), piezoelectric wafers (4), a base (5), and a lead electrode (6). Figure 2 shows the planar layout of the piezoelectric wafers within the sensor. In this layout, wafers No. 2, 4, and 6 are aligned tangentially and respond to normal loads, while wafers No. 1, 3, and 5 are also tangentially aligned and respond to tangential loads. Six sets of piezoelectric wafers are evenly distributed around the circumference at a specific initial angle.

The inertial mass block serves as the sensor's load response component, enabling the detection of six-dimensional acceleration. When subjected to six-dimensional acceleration, the inertial mass generates a corresponding six-dimensional inertial force/moment on the piezoelectric wafers. The charge signals produced are then converted into voltage signals through a charge amplifier, allowing the calculation of six-dimensional acceleration information from the sensor's six output signals.

III. LINEAR DECOUPLING

A. The decoupling principle

Let the output charges of the six groups of piezoelectric elements be denoted as Q_1, Q_2, Q_3, Q_4, Q_5, and Q_6. The charge sensitivities corresponding to these groups under linear acceleration A_i applied in the direction of the 6-DOF accelerometer i (where i=X, Y, Z) are represented as S_{Ai1}, S_{Ai2}, S_{Ai3}, S_{Ai4}, S_{Ai5}, and S_{Ai6}. When angular acceleration α_i is applied in the same direction, the charge sensitivities of the six groups of piezoelectric elements become $S_{\alpha i1}$, $S_{\alpha i2}$, $S_{\alpha i3}$, $S_{\alpha i4}$, $S_{\alpha i5}$, and $S_{\alpha i6}$, respectively. The displacement change induced by the inertial mass is linear over the sensor's measuring range. Consequently, in a composite acceleration field, the output charges from the dispatching chips corresponding to each dimension can be linearly summed, which can be expressed as Equation (1).

In practical measurements, to derive the acceleration signal in six dimensions from the six charge signals output by the sensor, Equation (1) must be transformed into Equation (2), which can further be expressed as Equation (3).

Here, S represents the sensor calibration matrix, S^{-1} denotes the sensor resolution matrix, and Q is the matrix of sensor output charge signals. After calibrating the 6-DOF accelerometer, the solution matrix is stored in the solver's solution module, allowing for the calculated six-dimensional acceleration to be obtained through linear operations.

B. Linear decoupling experiment

Figure 3 illustrates the linear decoupling schematic for the 6-DOF accelerometer. The experimental system comprises a shaker, a piezoelectric six-dimensional acceleration transducer, a charge amplifier, and a signal processing system.

Currently, there is no specialized calibration equipment or method specifically designed for 6-DOF accelerometers. Therefore, this experiment employs a method utilizing a linear and angular shaking table, equipped with a mounting fixture to apply six-dimensional acceleration. Linear acceleration is calibrated by comparison with a linear vibration table, while angular acceleration is calibrated using an angular vibration table, with the set values of the angular vibration table serving as the reference.

Figures 4 (a-c) depict the 6-DOF accelerometer and the linear and angular vibration table used in this experiment (provided by the 26th Research Institute of China Electronics Technology Group). Static calibration measurements for the 6-DOF accelerometer are conducted using LabVIEW software. The steps of the linear decoupling experiment are as follows:

- Loading Point Determination: The loading points are divided into 10 equal intervals within the operational range of the loading device and the 6-DOF accelerometer. Linear acceleration is assessed at 4 points ranging from 1 to 37, while angular acceleration is evaluated at 17.64 points, spanning from 17.64 to 335.12.
- Measurement Data Recording: Acceleration is

incrementally loaded from minimal to maximal values at the designated points. The calibration software records and averages 1000 measurements once the vibration stabilizes.

- Sensor Solution Matrix Calculation: Utilizing the calibration data, the calibration matrix and the solution matrix for the sensor are determined.
- Real-Time Measurement Experiment: The solution matrix is integrated into a 6-DOF accelerometry software system to conduct real-time measurements and assess the algorithm's effectiveness.

Figure 5 presents the input-output characteristic curve of the piezoelectric 6-DOF accelerometer. It is evident that under the influences of A_X, A_Y and A_Z, the input-output characteristics of each sensor channel, calibrated using a comparative method, exhibit linearity. In contrast, when subjected to angular accelerations α_X, α_Y and α_Z, the angular vibration table is utilized to establish the angular acceleration as the calibration standard. The input-output characteristics of the sensor demonstrate linearity only when the angular acceleration exceeds 125rad/s^2. This nonlinearity at lower angular acceleration values can be attributed primarily to a low signal-to-noise ratio and poor stability, compounded by the inherent nonlinearity of the angular shaker, which adversely affects the sensor's output. Consequently, data below 125rad/s^2 should be excluded from the calibration matrix processing.

Table I is the sensitivity of each output from the piezoelectric 6-DOF accelerometer, and it can be derived by linearly fitting the 36 input-output curves depicted in Figure 5. According to Table I, the calibration matrix S and the resolution matrix S^{-1} can be calculated using Equations 4 and 5. Tables II and III present the results of the linear decoupling solutions for both linear and angular acceleration. The experimental software environment utilized is MATLAB, while the hardware comprises an Intel(R) Core (TM) i5-3470 CPU with 12GB of installed memory. In this configuration, the solution time for the six directional outputs is 0.0000044 s, 0.0000040 s, 0.0000043 s, 0.0000042 s, 0.0000046 s, and 0.0000044 s, respectively. The reference error provided in the tables is calculated as the absolute error divided by the system measurement range, with the measurement ranges for the six directions being 0~37g, 0~37g, 0~37g, 0~335.12rad/s^2, 0~335.12rad/s^2, 0~335.12rad/s^2.

It is noteworthy that the decoupling error in the linear acceleration direction of the piezoelectric 6-DOF accelerometer is less than 0.3%, which is consistent with the sensor's linearity of better than 0.5%. In the angular acceleration direction, however, the decoupling error peaks at 14.15% in the section below 125rad/s^2, which does not align with the transducer's tangential and longitudinal load response linearity, also better than 0.5%. This suggests that the nonlinearity introduced by the angular shaker has resulted in a significant increase in calibration error. Although excluding data from the section below 125 rad/s^2 reduces the maximum error to 7.06%, the influence of the angular shaker's nonlinearity has not been completely mitigated.

IV. Decoupling Method Based on Cat Swarm BP Neural Network

A. Cat Swarm BP Neural Network

In practice, sensors are rarely completely linear. To reduce sensor decoupling errors, a decoupling effect test is performed using a Cat Swarm BP Neural Network. The BP neural network can have multiple input nodes, multiple output nodes, and several hidden layers between the input and output layers. As shown in Figure 6, the input layer consists of l neurons, the hidden layer has m neurons, and the output layer has n neurons. Each layer is connected via weights, and the network is trained using sample data to establish a nonlinear mapping relationship between the inputs and outputs. The Cat Swarm Optimization (CSO) algorithm is an optimization technique inspired by the behavioral patterns of cats. It simulates cats' hunting behavior, which includes two modes: seeking mode and tracing mode. The seeking mode has four key definitions: Search Memory Pool (SMP), Search Range of Dimension (SRD), Counts of Dimension to Change (CDC), and Self-Position Consideration (SPC). SMP refers to the size of the cat's memory pool, where the cat selects suitable positions from the memory pool. SRD indicates the search range in a particular dimension. CDC represents the number of dimensions each cat needs to change. SPC is a Boolean value (0 or 1) that determines whether the current position of the cat is included in the selection.

(1) The seeking mode consists of the following steps:

- Copy the current position of the cat into the memory pool.
- Adjust and modify each individual in the memory pool based on CDC and SRD, generating new individuals.
- Calculate the fitness of all individuals in the memory pool, where fitness evaluates the quality of the results.
- Select the individual with the best fitness to replace the current cat's position, completing the update.

(2) The tracing mode consists of the following steps:

- Update velocity:

$$v_{k,d}(t) = v_{k,d}(t-1) + r_1 \cdot c_1 \cdot [x_{best,d}(t-1) - x_{k,d}(t-1)]$$

where $v_{k,d}(t-1)$ is the velocity before the update, $v_{k,d}(t)$ is the updated velocity, $x_{best,d}(t-1)$ is the position of the best individual from the previous iteration, $x_{k,d}(t-1)$ is the current position, r_1 is a random number between 0 and 1, and c_1 is a constant defined based on specific conditions.

- Ensure the updated velocity remains within a given range, if it exceeds the range, replace it with the boundary value.
- Update position:

$$x_{k,d}(t) = x_{k,d}(t-1) + v_{k,d}(t)$$

(3) Overall algorithm process:

- First, initialize and generate the cat swarm.
- Divide the cat swarm into two modes, seeking mode and tracking mode, based on the grouping rate MR.
- Perform updates in the different modes.
- Calculate the fitness of each cat and select the best one.
- Check the termination condition and decide whether to continue looping.

B. Principle of Decoupling Based on Cat Swarm BP Neural Network

In the decoupling calculation, the piezoelectric six-dimensional accelerometer has 6 inputs, namely Q_1, Q_2, Q_3, Q_4, Q_5, Q_6, which correspond to the input layer neurons of the neural network. The outputs are also 6, namely A_X, A_Y, A_Z, α_X, α_Y, α_Z. To reduce computational complexity and interference from mutual coupling, the 6 outputs are trained separately, forming 6 independent networks. The BP neural network can have several hidden layers, but typically, one hidden layer is sufficient in most cases. M represents the number of neurons in the hidden layer. Currently, there is no definitive theory for selecting M, and it is generally determined by the empirical formula $M = \sqrt{m + n} + a$, where m is the number of neurons in the input layer, n is the number of neurons in the output layer, and a is a constant between 0 and 10. The designer then tests and selects the value. In this study, M=6 was chosen as the number of neurons in the hidden layer. The CSO algorithm was incorporated to modify the connection weights of the neural network, with parameters set as follows: SMP = 3, CDC = 0.2, SRD = 0.2, MR = 0.8. The cat swarm size and the number of training iterations were both set to 30, and the fitness function was the sum of the absolute errors of the output layer after normalization. The training used the neural network toolbox in MATLAB, and figure 7 show the training fitness curves for the 6 acceleration directions. The horizontal axis represents the number of iterations, the vertical axis represents the fitness, both are specific numerical values, and the curve represents the relationship between the fitness obtained and the number of iterations as the iterations increase.

C. Decoupling Experiment Based on Cat Swarm BP Neural Network

As can be seen from the figures, with the increase in the number of training iterations, the error decreases significantly, demonstrating the effectiveness of the method. However, it is also apparent that the training performance in the linear acceleration direction seems better than that in the angular acceleration direction. This is due to the sensitivity difference between linear and angular acceleration. The error in linear acceleration also influences the angular acceleration, leading to a more significant effect.

Using the trained network for testing, Table IV and V display the decoupling results and errors in the main directions under single-dimensional loading. Overall, the decoupling error based on the Cat Swarm BP Neural Network is lower than the error in linear decoupling, although there are still a few points where the decoupling performance is suboptimal. The largest reference error is around 1%.

V. Nonlinear decoupling

A. Principle based on nonlinear compensation

The input-output characteristics of the piezoelectric 6-DOF accelerometer exhibit nonlinearity due to factors such as calibration equipment, signal conditioning instruments, and the properties of piezoelectric materials. To enhance the measurement accuracy of the sensor, nonlinear correction and compensation are essential. In this study, a high-order polynomial fitting method based on the least squares technique is employed to model the input-output relationship of the sensor, followed by nonlinear compensation of the sensor's output.

For sensors with a single input and single output, the input value can be directly calculated using Equation (6) upon measuring the output value. However, for multi-input multi-output sensors, the relationship between inputs and outputs is not a straightforward one-to-one correspondence but rather a many-to-many mapping. Therefore, the fitted high-order polynomials cannot be directly used to compute input values when output values are known.

To address this complexity, we propose an iterative decoupling method that employs nonlinear compensation in conjunction with linear decoupling. Figure 8 illustrates the flowchart of the adaptive decoupling algorithm based on nonlinear compensation. The steps of this method are as follows:

(1) Based on the calibration experimental data, the sensor's sensitivity is linearly fitted using the least squares method, resulting in the sensitivity matrix S and the calibration matrix S^{-1}.

(2) Utilizing the calibration data, higher-order polynomial fitting yields 36 input-output curves for the piezoelectric crystal group under six-dimensional acceleration loading. These curve equations are represented in the matrix of higher-order equations L (Equation 7), simplified as Equation (8). Each input-output curve in L is expressed as an eighth-order curve equation as shown in Equation (6). Where α_8, α_7, α_6, α_5, α_4, α_3, α_2, α_1, α_0, are the coefficient of the polynomial, which do not involve integration and can be uniquely obtained by simple linear operations.

(3) Using the sensor's output value Q and the calibration matrix S^{-1}, the acceleration input value A can be computed via Equation (3).

(4) The acceleration input value A derived in step (3) is substituted into the respective six curves to obtain the output value for each curve at the current acceleration input. This output value is then divided by the input to recover the 36 sensitivities, which replace the previous linear fit. This results in a new calibration matrix S, denoted as the adaptive sensitivity matrix S_1. The solving matrix S_1^{-1} is also computed, referred to as the adaptive solving matrix S_1'. The replacement update process can be expressed by Equation (9).

Take the acceleration in the X direction as an example: L_{AX} represents the high-order fitting curve of the input and output of the piezoelectric wafer when the linear acceleration in the X direction is loaded in a single dimension; L_{AX} (A_X) means that the A_X that has been calculated by linear decoupling is substituted into the higher-order fitting curve L_{AX} to obtain the ordinate of A_X in L_{AX}. $L_{AX}(A_X)/A_X$ is the recalculated sensitivity in the current initial solution state, and so on to obtain 36 new sensitivities.

(5) Steps (3) and (4) are repeated, replacing the old calibration matrix with the new one, until the error falls below a predetermined threshold or after a specified number of iterations.

Figure 9 presents a graph depicting the citation error as a function of the number of iterations in the directional solving process. The citation error is recorded at 0.03% when no iterations are performed. After the first iteration, the citation error decreases to 0.0014243%, and following the second iteration, it further reduces to 0.0010885%. While subsequent iterations continue to improve the error, the enhancements become less pronounced. To optimize solving efficiency, the experiment is limited to two iterations.

In MATLAB software environment, utilizing an Intel(R)

Core (TM) i5-3470 CPU with 12GB of installed memory, the adaptive decoupling operation time for nonlinear compensation is measured at 0.00047 seconds. This demonstrates the high precision and efficiency of the adaptive decoupling algorithm utilizing nonlinear compensation.

Tables VI and VII present the nonlinear decoupling results for the 6-DOF accelerometer in each direction after 2 iterations. The decoupling error in the linear acceleration direction is found to be less than 0.0318%. Furthermore, when excluding data from the angular acceleration segment below 125 rad/s^2, specifically with α_x=335.12 rad/s^2 and α_Y=335.12 rad/s^2 (which are classified as coarse errors according to the Grabs criterion after reviewing the raw voltage data), the decoupling errors in the angular acceleration direction are all below 1%.

B. Discussion of decoupling effects

Figure 10 illustrates a comparison of the quoted errors among linear decoupling, neural network decoupling, and nonlinear compensation decoupling methods under varying loading values. All metrics for the three decoupling algorithms were obtained in a MATLAB software environment, utilizing an Intel(R) Core (TM) i5-3470 CPU with 12GB of installed memory. Table VIII presents the decoupling parameters for the neural network algorithm, while Table IX compares the solving time, average solving error for linear acceleration, average solving error for angular acceleration, and the deviation degree of the three decoupling algorithms. The deviation degree d is calculated using Equation (10), where a smaller deviation indicates a more stable overall decoupling method with reduced fluctuations. In this formula, A_x', A_Y', A_z', α_x', α_Y', α_z' represent the solution values for each direction, and A_x, A_Y, A_z, α_x, α_Y, α_z denote the true values for each direction.

The error associated with the nonlinear compensation decoupling algorithm is significantly lower than that of the linear and neural network decoupling algorithms. Specifically, the average reference error for linear acceleration decreases from 0.1170% and 0.0690% to 0.0067%, while the average reference error for angular acceleration drops from 6.0185% and 2.2899% to 0.8989%. In terms of solving time, the linear decoupling algorithm requires 0.000004 seconds, the neural network decoupling algorithm takes 0.02458 seconds, and the nonlinear compensation decoupling algorithm operates at 0.00047 seconds. Although the solving time for the nonlinear compensation algorithm is longer than that of the linear decoupling algorithm, it remains significantly shorter than that of the neural network decoupling algorithm, thus meeting the demands for real-time measurement.

VI. CONCLUSIONS

This paper investigates the linear and nonlinear decoupling methods for the piezoelectric six-dimensional acceleration sensor, comparing and analyzing the effects of linear decoupling, neural network decoupling, and nonlinear adaptive decoupling algorithms. The experiments demonstrate that the nonlinear adaptive decoupling method can effectively enhance solving accuracy while fulfilling real-time measurement requirements within a MATLAB software environment and an Intel(R) Core (TM) i5-3470 CPU with 12GB of installed memory. The key findings of this research are as follows:

(1) The proposed nonlinear compensation adaptive decoupling model shows significant improvement over the traditional linear decoupling model, with the average solving error for linear acceleration reduced from 0.1170% to 0.0067%, and for angular acceleration from 6.0185% to 0.8989%. While the decoupling time increases from 0.000004 seconds to 0.00047 seconds, it remains sufficient for real-time measurement needs.

(2) Compared to the neural network decoupling model, the average solution error for linear acceleration decreases from 0.0690% to 0.0067%, and for angular acceleration from 2.2899% to 0.8989%. In the same environment, the settling time for nonlinear compensation adaptive decoupling is 0.00047 seconds, significantly shorter than the 0.02458 seconds required for neural network decoupling. This indicates that the nonlinear compensation decoupling method is more efficient and accurate, making it more suitable for practical applications.

(3) While high-order polynomial curve fitting is effective, it may not always represent the optimal method. Overly complex fittings can lead to overfitting, wherein the iterative process becomes trapped in local optimal solutions. Future research should focus on exploring alternative fitting methods or developing new algorithms, while remaining cautious of the potential impact on the real-time measurement capabilities of the sensor.

Appendix

The formulas, figures, and tables utilized in this article are summarized as follows. The first list includes Figures 1 to 10, which are referenced throughout the paper. Notably, Figure 5 and 7 are positioned after Figure 9 due to its larger size.

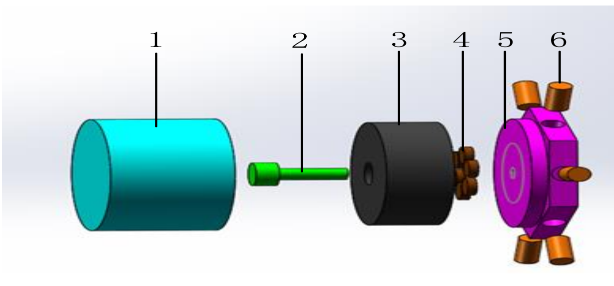

Fig. 1. Schematic diagram of piezoelectric six-axis accelerometer.

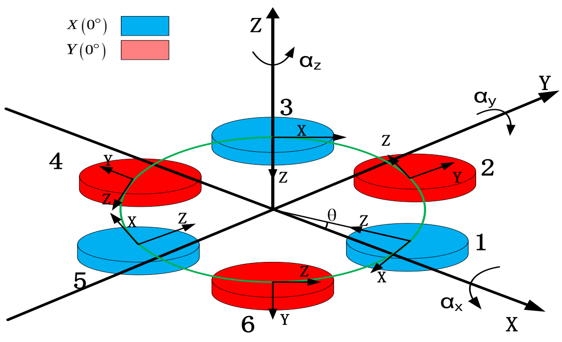

Fig. 2. Piezoelectric element layout.

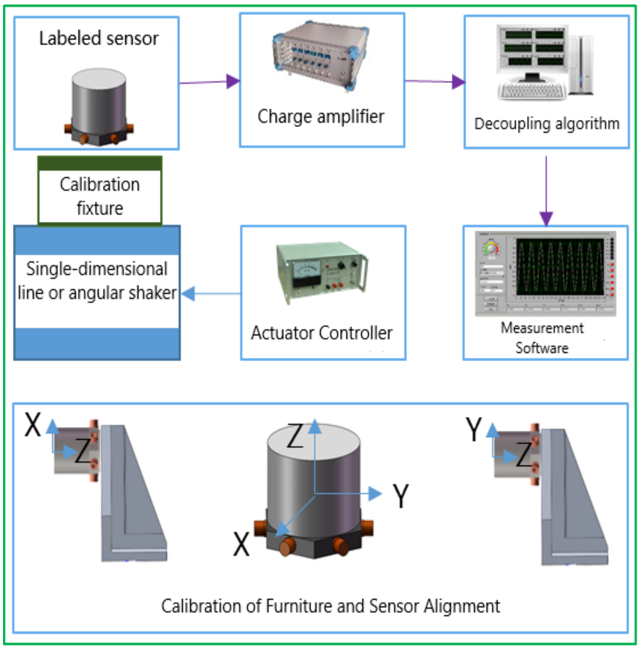

Fig. 3. Schematic diagram of linear decoupling experiment.

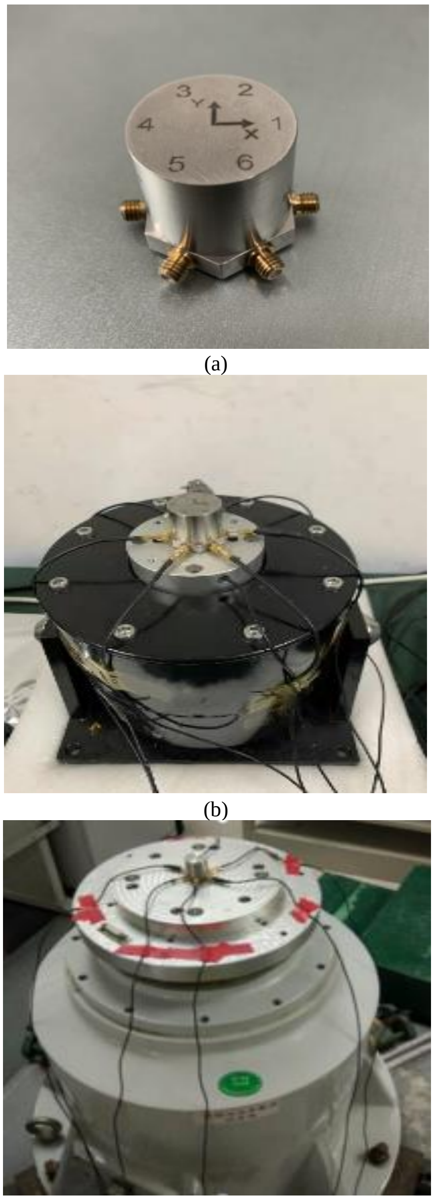

(a)

(b)

(c)

Fig. 4. (a) Six-axis accelerometer; (b) Line vibrator; (c) Angular vibrato.

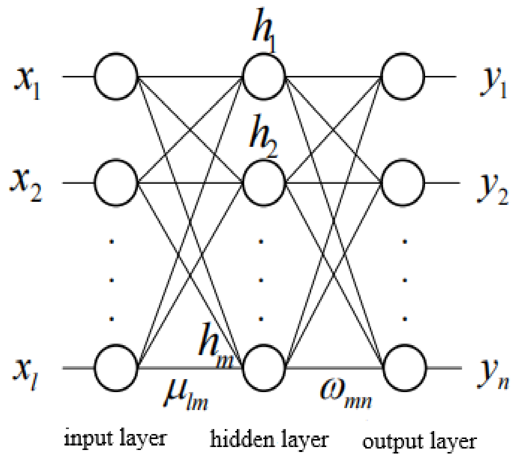

Fig. 6. 3-layer BP network.

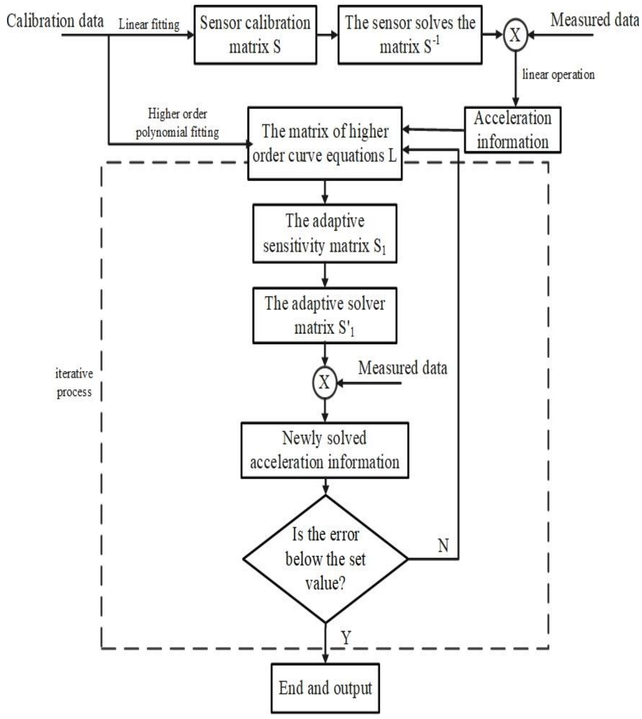

Fig. 8. Input-output characteristics curves of piezoelectric six-axis accelerometer prototype.

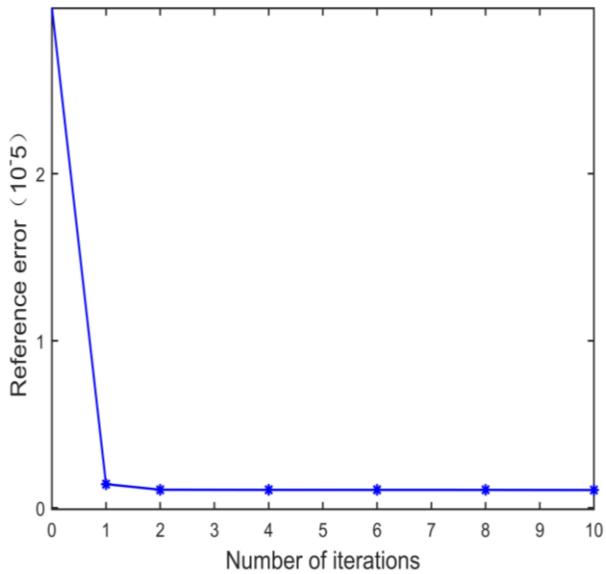

Fig. 9. The relation curve between the calculation error and the number of iterations in A_X direction.

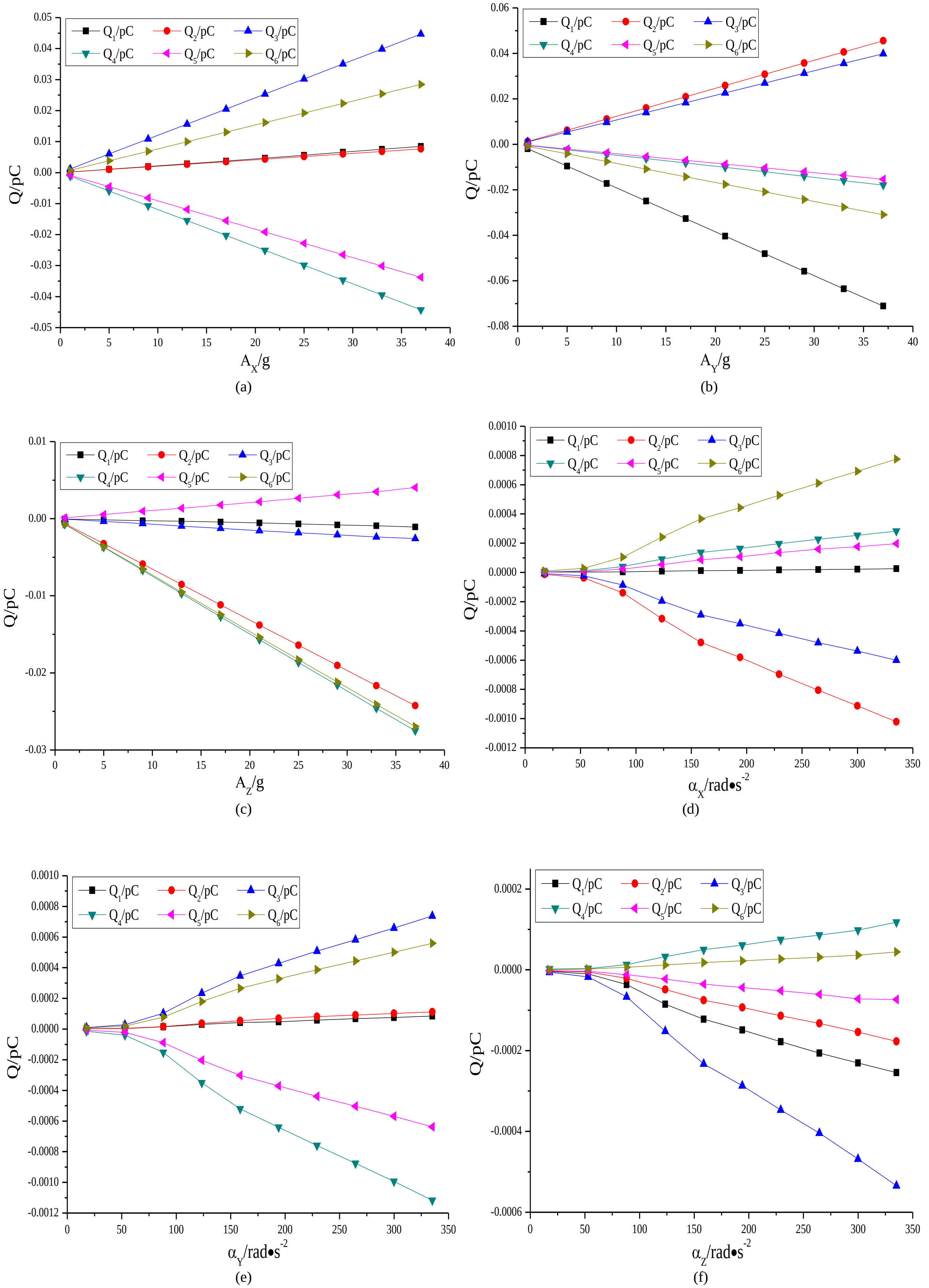

Fig. 5. (a) Input-output characteristics of A_X; (b) Input-output characteristics of A_Y; (c) Input-output characteristics of A_Z; (d) Input-output characteristics of α_X; (e) Input-output characteristics of α_Y; (f) Input-output characteristics of α_Z.

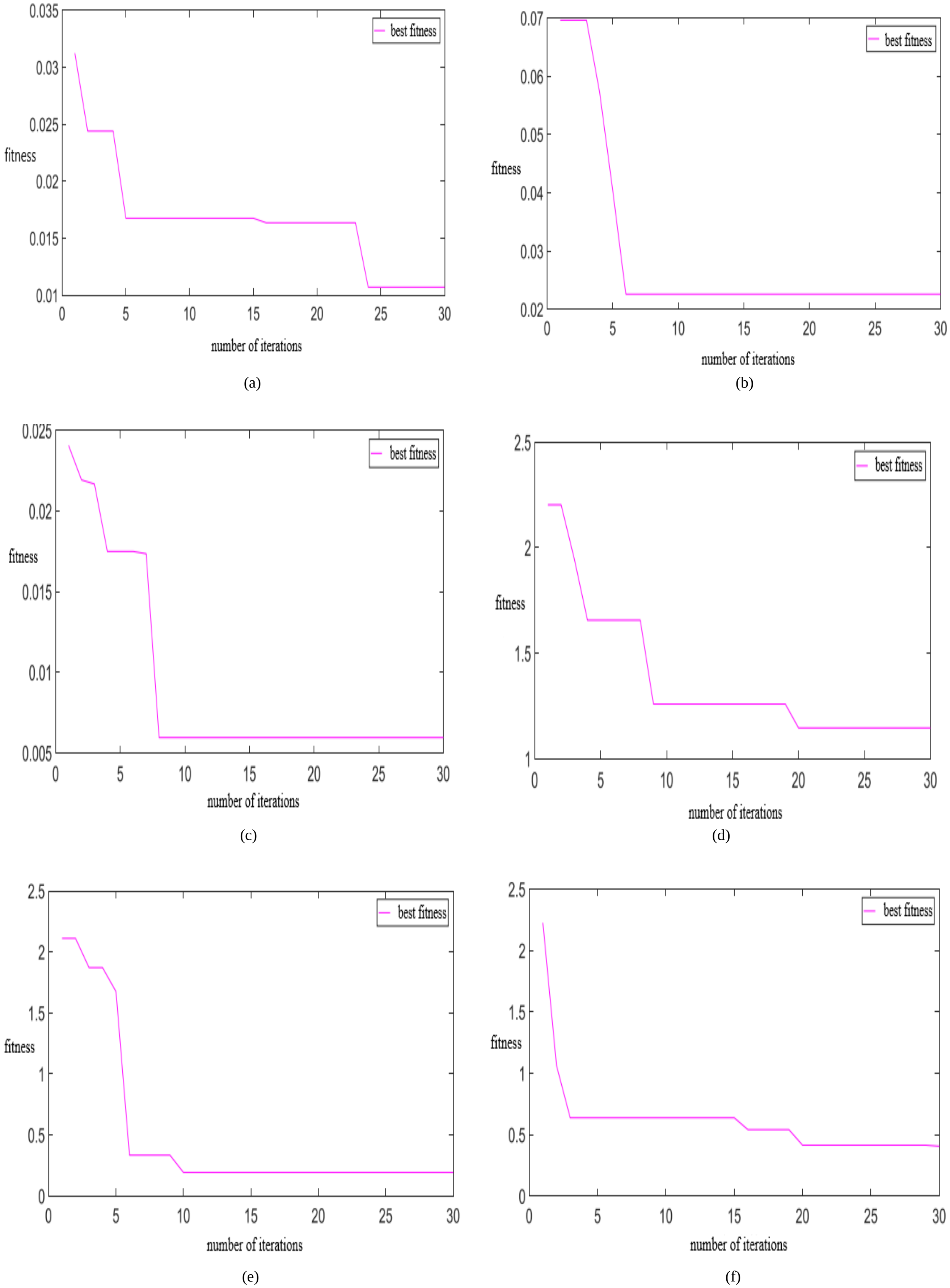

Fig. 7. (a) Training diagram of A_X-axis; (b) Training diagram of A_Y-axis; (c) Training diagram of A_Z-axis; (d) Training diagram of α_X-axis; (e) Training diagram of α_Y-axis; (f) Training diagram of α_Z-axis.

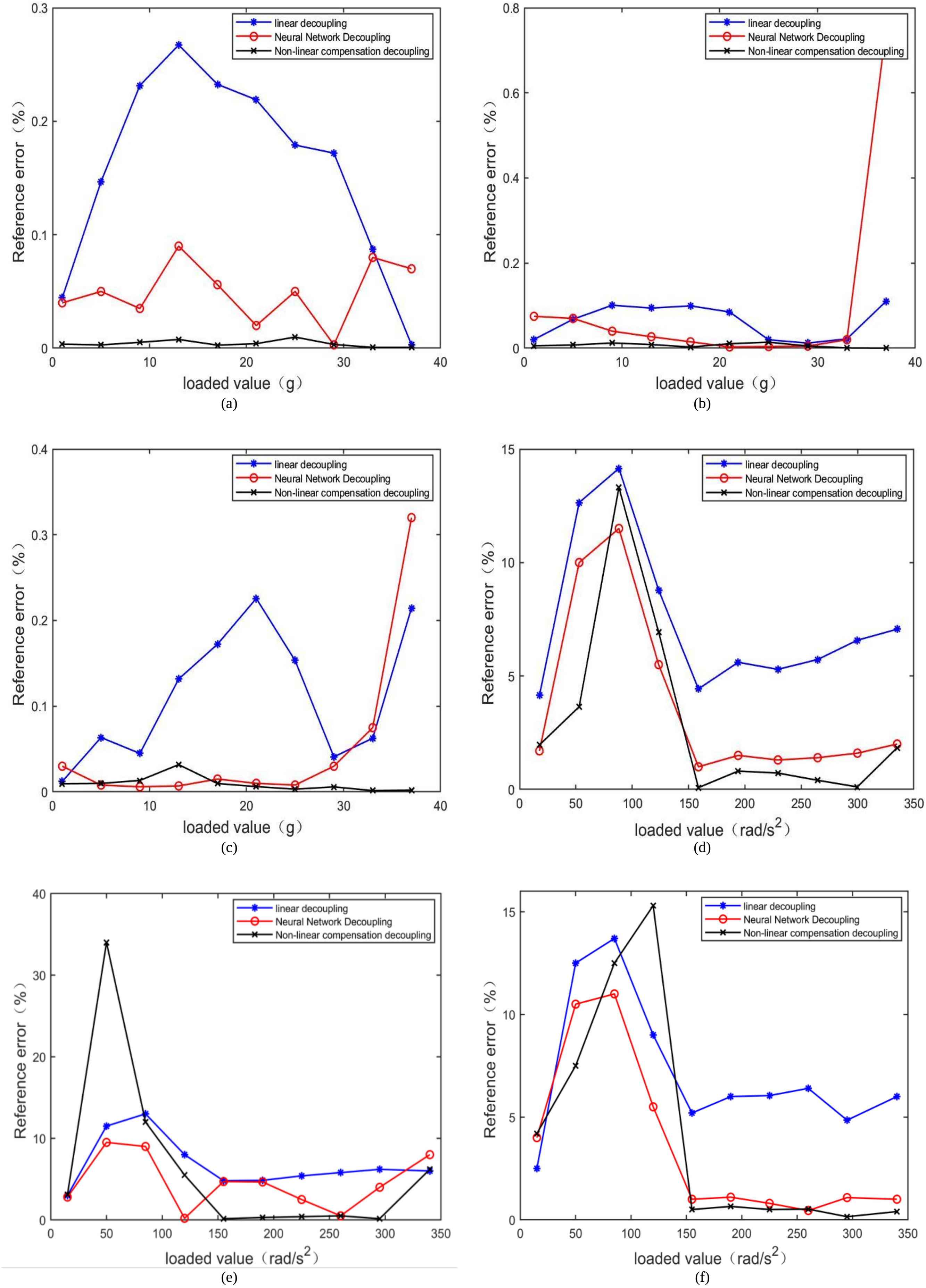

Fig. 10. (a) Comparison of decoupling effects in the A_X-direction; (b) Comparison of decoupling effects in the A_Y-direction; (c) Comparison of decoupling effects in the A_Z-direction; (d) Comparison of decoupling effects in the α_X-direction; (e) Comparison of decoupling effects in the α_Y-direction; (f) Comparison of decoupling effects in the α_Z-direction.

The second list is equation (1) to (10), which are used in this article. Because the equation (4) and (5) are too long, they are placed after equation (9).

$$\begin{bmatrix} Q_1 \\ Q_2 \\ Q_3 \\ Q_4 \\ Q_5 \\ Q_6 \end{bmatrix} = \begin{bmatrix} S_{A_X 1} & S_{A_Y 1} & S_{A_Z 1} & S_{\alpha_X 1} & S_{\alpha_Y 1} & S_{\alpha_Z 1} \\ S_{A_X 2} & S_{A_Y 2} & S_{A_Z 2} & S_{\alpha_X 2} & S_{\alpha_Y 2} & S_{\alpha_Z 2} \\ S_{A_X 3} & S_{A_Y 3} & S_{A_Z 3} & S_{\alpha_X 3} & S_{\alpha_Y 3} & S_{\alpha_Z 3} \\ S_{A_X 4} & S_{A_Y 4} & S_{A_Z 4} & S_{\alpha_X 4} & S_{\alpha_Y 4} & S_{\alpha_Z 4} \\ S_{A_X 5} & S_{A_Y 5} & S_{A_Z 5} & S_{\alpha_X 5} & S_{\alpha_Y 5} & S_{\alpha_Z 5} \\ S_{A_X 6} & S_{A_Y 6} & S_{A_Z 6} & S_{\alpha_X 6} & S_{\alpha_Y 6} & S_{\alpha_Z 6} \end{bmatrix} \begin{bmatrix} A_X \\ A_Y \\ A_Z \\ \alpha_X \\ \alpha_Y \\ \alpha_Z \end{bmatrix} \tag{1}$$

$$\begin{bmatrix} A_X \\ A_Y \\ A_Z \\ \alpha_X \\ \alpha_Y \\ \alpha_Z \end{bmatrix} = \begin{bmatrix} S_{A_X 1} & S_{A_Y 1} & S_{A_Z 1} & S_{\alpha_X 1} & S_{\alpha_Y 1} & S_{\alpha_Z 1} \\ S_{A_X 2} & S_{A_Y 2} & S_{A_Z 2} & S_{\alpha_X 2} & S_{\alpha_Y 2} & S_{\alpha_Z 2} \\ S_{A_X 3} & S_{A_Y 3} & S_{A_Z 3} & S_{\alpha_X 3} & S_{\alpha_Y 3} & S_{\alpha_Z 3} \\ S_{A_X 4} & S_{A_Y 4} & S_{A_Z 4} & S_{\alpha_X 4} & S_{\alpha_Y 4} & S_{\alpha_Z 4} \\ S_{A_X 5} & S_{A_Y 5} & S_{A_Z 5} & S_{\alpha_X 5} & S_{\alpha_Y 5} & S_{\alpha_Z 5} \\ S_{A_X 6} & S_{A_Y 6} & S_{A_Z 6} & S_{\alpha_X 6} & S_{\alpha_Y 6} & S_{\alpha_Z 6} \end{bmatrix}^{-1} \begin{bmatrix} Q_1 \\ Q_2 \\ Q_3 \\ Q_4 \\ Q_5 \\ Q_6 \end{bmatrix} \tag{2}$$

$$A = S^{-1} Q \tag{3}$$

$$Y = a_8 x^8 + a_7 x^7 + a_6 x^6 + a_5 x^5 + a_4 x^4 + a_3 x^3 + a_2 x^2 + a_1 x^1 + a_0 x^0 \tag{6}$$

$$L = \begin{bmatrix} L_{A_X 1} & L_{A_X 2} & L_{A_X 3} & L_{A_X 4} & L_{A_X 5} & L_{A_X 6} \\ L_{A_Y 1} & L_{A_Y 2} & L_{A_Y 3} & L_{A_Y 4} & L_{A_Y 5} & L_{A_Y 6} \\ L_{A_Z 1} & L_{A_Z 2} & L_{A_Z 3} & L_{A_Z 4} & L_{A_Z 5} & L_{A_Z 6} \\ L_{\alpha_X 1} & L_{\alpha_X 2} & L_{\alpha_X 3} & L_{\alpha_X 4} & L_{\alpha_X 5} & L_{\alpha_X 6} \\ L_{\alpha_Y 1} & L_{\alpha_Y 2} & L_{\alpha_Y 3} & L_{\alpha_Y 4} & L_{\alpha_Y 5} & L_{\alpha_Y 6} \\ L_{\alpha_Z 1} & L_{\alpha_Z 2} & L_{\alpha_Z 3} & L_{\alpha_Z 4} & L_{\alpha_Z 5} & L_{\alpha_Z 6} \end{bmatrix} \tag{7}$$

$$L = \left[L_{AX} L_{AY} L_{AZ} L_{\alpha X} L_{\alpha Y} L_{\alpha Z} \right]^T \tag{8}$$

$$S_1 = \begin{bmatrix} \dfrac{L_{A_X}(A_X)}{A_X} \\ \dfrac{L_{A_Y}(A_Y)}{A_Y} \\ \dfrac{L_{A_Z}(A_Z)}{A_Z} \\ \dfrac{L_{\alpha_X}(\alpha_X)}{\alpha_X} \\ \dfrac{L_{\alpha_Y}(\alpha_Y)}{\alpha_Y} \\ \dfrac{L_{\alpha_Z}(\alpha_Z)}{\alpha_Z} \end{bmatrix} \tag{9}$$

$$S = \begin{bmatrix} 2.2910E-04 & 2.0726E-04 & 1.2088E-03 & -1.1963E-03 & -9.1292E-04 & 7.6942E-04 \\ -1.9241E-03 & 1.2318E-03 & 1.0779E-03 & -4.8432E-04 & -4.1488E-04 & -8.3676E-04 \\ -2.8144E-05 & -6.5640E-04 & -7.1163E-05 & -7.4483E-04 & 1.0748E-04 & -7.2944E-04 \\ 7.6305E-08 & -3.2765E-06 & -1.9335E-06 & 9.1219E-07 & 6.3776E-07 & 2.4870E-06 \\ 2.6660E-07 & 3.6326E-07 & 2.3676E-06 & -3.5753E-06 & -2.0510E-06 & 1.8013E-06 \\ -8.2363E-07 & -5.5556E-07 & -1.6865E-06 & 3.6384E-07 & -2.4357E-07 & 1.3308E-07 \end{bmatrix} \tag{4}$$

$$S^{-1} = \begin{bmatrix} 334.19590 & -496.762011 & 43.4300147 & -183534.935 & -101633.473 & -12054.0342 \\ -1723.79271 & -84.421915 & -752.916256 & -209940.322 & 686035.55 & -53929.087 \\ 1249.0773 & 259.943948 & 212.54991 & 149008.821 & -501730.259 & -415685.206 \\ 2049.69376 & 50.2318284 & -66.4189283 & 31864.0170 & -934558.834 & 155510.111 \\ -3431.23192 & 171.393964 & -385.566120 & 213902.634 & 1163617.07 & -945190.953 \\ -1182.08788 & 43.7376788 & -704.790869 & 180442.928 & 561260.051 & -208513.537 \end{bmatrix} \tag{5}$$

$$d = \sum \left(\frac{\left| A_{Xi}{}' - A_{Xi} \right|}{A_{Xi}} + \frac{\left| A_{Yi}{}' - A_{Yi} \right|}{A_{Yi}} + \frac{\left| A_{Zi}{}' - A_{Zi} \right|}{A_{Zi}} + \frac{\left| \alpha_{Xi}{}' - \alpha_{Xi} \right|}{\alpha_{Xi}} + \frac{\left| \alpha_{Yi}{}' - \alpha_{Yi} \right|}{\alpha_{Yi}} + \frac{\left| \alpha_{Zi}{}' - \alpha_{Zi} \right|}{\alpha_{Zi}} \right) \tag{10}$$

The third list is table I to IX, which are used in this article.

TABLE I
THE OUTPUT SENSITIVITY OF EACH PIEZOELECTRIC CHIP OF THE PIEZOELECTRIC 6-DEGREE-OF-FREEDOM ACCELEROMETER

Sensitivity	Channel 1	Channel 2	Channel 3	Channel 4	Channel 5	Channel 6
A_X (pC/g)	2.2910E-04	2.0726E-04	1.2088E-03	-1.1963E-03	-9.1292E-04	7.6942E-04
A_Y (pC/g)	-1.9241E-03	1.2318E-03	1.0779E-03	-4.8432E-04	-4.1488E-04	-8.3676E-04
A_Z (pC/g)	-2.8144E-05	-6.5640E-04	-7.1163E-05	-7.4483E-04	1.0748E-04	-7.2944E-04
α_X $(pC/rad{\cdot}s^{-2})$	7.6305E-08	-3.2765E-06	-1.9335E-06	9.1219E-07	6.3776E-07	2.4870E-06
α_Y $(pC/rad{\cdot}s^{-2})$	2.6660E-07	3.6326E-07	2.3676E-06	-3.5753E-06	-2.0510E-06	1.8013E-06
α_X $(pC/rad{\cdot}s^{-2})$	-8.2363E-07	-5.5556E-07	-1.6865E-06	3.6384E-07	-2.4357E-07	1.3308E-07

TABLE II
THE LINEAR DECOUPLING SOLUTION FOR LINEAR ACCELERATION RESULTS

Input value (g)	A_X		A_Y		A_Z	
	Solved value (g)	Reference error	Solved value (g)	Reference error	Solved value (g)	Reference error
1	1.0164	0.0444%	0.9924	0.0206%	0.9955	0.0122%
5	5.0543	0.1468%	4.9748	0.0681%	4.9765	0.0635%
9	9.0857	0.2315%	8.9626	0.1010%	8.9834	0.0449%
13	13.0989	0.2672%	12.9651	0.0943%	13.0487	0.1317%
17	17.0860	0.2325%	16.9632	0.0995%	17.0637	0.1723%
21	21.0810	0.2189%	20.9685	0.0852%	21.0835	0.2257%
25	25.0662	0.1790%	24.9927	0.0197%	25.0567	0.1533%
29	29.0636	0.1719%	28.9956	0.0120%	29.0151	0.0409%
33	33.0322	0.0871%	33.0082	0.0220%	33.0232	0.0627%
37	37.0011	0.0030%	36.9592	0.1102%	36.9206	0.2145%

TABLE III
THE LINEAR DECOUPLING SOLUTION FOR ANGULAR ACCELERATION RESULTS

Input value (rad/s^2)	α_X		α_Y		α_Z	
	Solved value (rad/s^2)	Reference error	Solved value (rad/s^2)	Reference error	Solved value (rad/s^2)	Reference error
17.64	3.7437	4.147%	5.7049	3.561%	4.9055	3.800%
52.91	10.5375	12.644%	12.7590	11.981%	11.2851	12.421%
88.19	40.7736	14.149%	42.1413	13.741%	41.5382	13.921%
123.46	94.0128	8.787%	95.9174	8.219%	91.1027	9.655%
158.74	143.8893	4.431%	143.2706	4.616%	139.8109	5.648%
194.02	175.2428	5.603%	177.9403	4.798%	172.4619	6.433%
229.29	211.5531	5.293%	210.9696	5.467%	207.6498	6.457%
264.57	245.3812	5.726%	244.9468	5.856%	242.1452	6.692%
299.84	277.7967	6.578%	278.8106	6.275%	281.5519	5.457%
335.12	311.4537	7.062%	314.5417	6.141%	313.5342	6.441%

TABLE IV
THE LINEAR ACCELERATION RESULTS SOLVED THROUGH DECOUPLING BASED ON A CAT SWARM BP NEURAL NETWORK

Input value (g)	A_X		A_Y		A_Z	
	Solved value (g)	Reference error	Solved value (g)	Reference error	Solved value (g)	Reference error
1	0.963055	0.100%	0.977164	0.062%	0.996391	0.010%
5	4.976881	0.062%	4.959129	0.110%	4.998509	0.004%
9	8.975494	0.066%	9.006661	0.018%	8.994228	0.016%
13	12.9565	0.118%	13.01338	0.036%	13.01118	0.030%
17	16.93573	0.174%	16.99279	0.019%	17.01589	0.043%
21	20.93118	0.186%	21.00299	0.008%	21.02475	0.067%
25	24.95504	0.122%	24.99719	0.008%	25.02033	0.055%
29	28.98843	0.031%	29.00497	0.013%	29.03098	0.084%
33	32.99531	0.013%	33.00142	0.004%	33.03731	0.101%
37	36.88027	0.324%	36.9981	0.005%	37.03667	0.099%

TABLE V
THE ANGULAR ACCELERATION RESULTS SOLVED THROUGH DECOUPLING BASED ON A CAT SWARM BP NEURAL NETWORK

Input value (rad/s^2)	α_X		α_Y		α_Z	
	Solved value (rad/s^2)	Reference error	Solved value (rad/s^2)	Reference error	Solved value (rad/s^2)	Reference error
194.02	191.9684	0.612%	193.3083	0.212%	191.0059	0.899%
229.29	228.1874	0.329%	229.9041	0.183%	226.1936	0.924%
264.57	263.3018	0.378%	264.4417	0.038%	264.1043	0.139%
299.84	300.2293	0.116%	299.5057	0.100%	300.0306	0.057%
335.12	335.5328	0.123%	335.1694	0.015%	338.5377	1.020%

TABLE VI
THE LINEAR ACCELERATION RESULTS SOLVED THROUGH ADAPTIVE DECOUPLING BASED ON NONLINEAR COMPENSATION

Input value (g)	A_X		A_Y		A_Z	
	Solved value (g)	Reference error	Solved value (g)	Reference error	Solved value (g)	Reference error
1	1.0013	0.0036%	0.9980	0.0055%	0.9965	0.0095%
5	4.9989	0.0029%	5.0028	0.0075%	5.0037	0.0099%
9	9.0019	0.0052%	8.9955	0.0123%	8.9950	0.0134%
13	12.9972	0.0077%	13.0032	0.0086%	13.0118	0.0318%
17	17.0010	0.0027%	17.0010	0.0027%	16.9964	0.0098%
21	21.0015	0.0040%	20.9961	0.0105%	21.0023	0.0062%
25	24.9964	0.0098%	25.0053	0.0142%	25.0012	0.0032%
29	29.0012	0.0033%	28.9981	0.0050%	29.0022	0.0059%
33	32.9997	0.0007%	33.0003	0.0007%	33.0006	0.0015%
37	37.0000	0.0001%	36.9979	0.0003%	36.9993	0.0020%

TABLE VII
THE ANGULAR ACCELERATION RESULTS SOLVED THROUGH ADAPTIVE DECOUPLING BASED ON NONLINEAR COMPENSATION.

Input value (rad/s^2)	α_X		α_Y		α_Z	
	Solved value (rad/s^2)	Reference error	Solved value (rad/s^2)	Reference error	Solved value (rad/s^2)	Reference error
17.64	11.0625	1.963%	4.4046	3.949%	4.2281	4.002%
52.91	65.1357	3.648%	169.6561	34.837%	78.8232	7.732%
88.19	43.5962	13.307%	45.8789	12.626%	45.2023	12.828%
123.46	102.5511	6.931%	104.8864	5.542%	71.9010	15.385%
158.74	158.4649	0.0821%	158.2184	0.156%	157.2985	0.430%
194.02	191.3080	0.809%	192.6065	0.422%	191.7406	0.680%
229.29	231.7132	0.723%	230.6243	0.398%	230.6541	0.407%
264.57	263.2156	0.404%	263.1548	0.422%	263.2265	0.401%
299.84	300.2198	0.113%	300.0717	0.069%	299.7254	0.034%
335.12	328.9536	1.840%	313.5429	6.439%	334.0372	0.3223%

TABLE VIII
NEURAL NETWORK DECOUPLING ALGORITHM PARAMETERS

Number of neurons in hidden layer	memory pool	domain of variation	variable	classification rate
6	3	0.2	0.2	0.8

TABLE IX
PERFORMANCE COMPARISON OF THREE TYPES OF DECOUPLING ALGORITHMS

Decoupling algorithm	Linear decoupling	Neural network decoupling	Nonlinear compensation decoupling
Solution time	0.000004s	0.02458s	0.00047s
Average linear acceleration solution error	0.1170%	0.0690%	0.0067%
Average angular acceleration solution error	6.0185%	2.2899%	0.8989%
Degree of deviation	1.52683	0.67994	0.15672

REFERENCES

[1] Zhao, C.L. (2020), “Design and application of six-degree-of-freedom flight test system for rotary-wing UAVs”, Computer Applications and Software, 37(3): 72-77.

[2] Cai, Z.Y., Zhou, L.K., Huang, H.Z., et al. (2023), "Study on Soft Fault Detection Method for Redundant Strapdown Inertial Navigation Systems," Journal of Electronic Measurement and Instrumentation, 37(10): 115-122.

[3] Li, C.G., Wang, Y., Chen, J. (2018), “Fault Diagnosis in a Gyroscope-Based Six-Axis Accelerometer”, Transactions of Famena, 4(3): 103-114.

[4] Ghasemzadeh, V., Arefi, M. M. (2017), “Design Modelling and Simulation of an INS System Using an Asymmetric Structure of Six Accelerometers and Its Error Analysis in the ECEF Frame”, Proceedings of the Institution of Mechanical Engineers Part G-Journal of Aerospace Engineering, 231(13): 2345-2361.

[5] Cheng, X., Quan, S., Deng, J.Q. (2017), “Application of angular accelerometer in vehicle/underwater vehicle guidance and control system”, Navigation Position and Timing, 4(5): 60-64.

[6] Liu, Y.P., Wang, X., You, J.J., et al. (2020), “Ocean Wave Buoy Based on Parallel Six-Dimensional Accelerometer”, IEEE Access, 8: 29627-29638.

[7] Yu, C.Z., Liu, J.H., Sun, Z.B. (2015), “Research on the dynamic characteristics of parallel six-axis accelerometer based on Kane’s method”, Chinese Journal of Scientific Instrument, 36(7): 1611-1617.

[8] Du, C.X., Tang, J.G., Yu, C.Z., et al. (2020), “Isotropy analysis of parallel six-axis accelerometer on circular hyperboloids”, International Journal of Circuits, Systems and Signal Processing, 14: 222-231.

[9] Hao, Z., Yu, C.Z., Zhang, J.L., et al. (2023), “Nonlinear decoupling of parallel six-dimensional accelerometer based on SSA-GB-ELM”, Journal of Electronic Measurement and Instrumentation, 37(10): 106-114.

[10] You, J.J., Li, C.G., Wu, H.T., et al. (2017), "Research on Decoupling Algorithm for Pre-tightened Parallel Six-Dimensional Acceleration Sensor," Journal of Instruments, 38(05): 1216-1225. DOI: 10.19650/j.cnki.cjsi.2017.05.021.

[11] You, J.J., Li, C.G., Wu, H.T., et al. (2015), “Hybrid decoupling algorithm and error auto-compensation algorithm of the parallel type six-axis accelerometer”, Chinese Journal of Scientific Instrument, 36(10) :2249-2257.

[12] You, J.J., Wang, L.K., Xi, F.F., et al. (2020), “Decoupling algorithm and maximum operation frequency of a novel parallel type six-axis accelerometer”, IEEE Sensors Journal, 20(21): 12637-12651.

[13] Zhang, X.Z., You, J.J., Jiang, J.F., et al. (2024), “Configuration synthesis of fully isotropic Stewart-type six-dimensional acceleration sensing mechanism”, Journal of Nanjing University of Aeronautics and Astronautics, 56(4): 723-730.

[14] Zhang, X.Z., You, J.J., Zhang, Y.W. (2024), “Derivation of output coordination equations for several typical parallel six-dimensional acceleration sensing mechanisms (in English)”, Transactions of Nanjing University of Aeronautics and Astronautics, 2024(S1): 96-102.

[15] Liu, J., Xu, J.L., Li, M., et al. (2019), "Static Sensitivity Analysis of Washer-type Piezoelectric Six-Dimensional Force Sensor," Optics and Precision Engineering, 27(04): 901-910.

[16] Zhang, D.Z., Liu, J., Qin, L., et al. (2020), “Multiparameter Modelling of Piezoelectric Six-Degree-of-Freedom Accelerometer About Sensitivity Characteristics”, IEEE Sensors Journal, 20(13): 7129-7137.

[17] Zhang, D., Li, M., Qin, L., et al. (2021), “Analytical Modeling of Piezoelectric 6-Degree-of-Freedom Accelerometer About Cross-Coupling Degree”, Measurement, 181: 109630.